Estimating global ammonia (NH₃) emissions based on IASI observations from 2008 to 2018

Zhenqi Luo[1, 2], Yuzhong Zhang[1, 2, *], Wei Chen[1, 2], Martin van Damme[3, 4], Pierre-François Coheur[3], Lieven Clarisse[3]

[1]Key Laboratory of Coastal Environment and Resources of Zhejiang Province, School of Engineering, Westlake University, Hangzhou, Zhejiang Province, 310024, China
[2]Institute of Advanced Technology, Westlake Institute for Advanced Study, Hangzhou, Zhejiang Province, 310024, China
[3]Université libre de Bruxelles (ULB), Spectroscopy, Quantum Chemistry and Atmospheric Remote Sensing (SQUARES), Brussels, Belgium
[4]BIRA-IASB - Belgian Institute for Space Aeronomy, Brussels, Belgium

Correspondence to: Y. Zhang (zhangyuzhong@westlake.edu.cn), Z. Luo (zl725@cornell.edu)

Abstract. Emissions of ammonia (NH₃) to the atmosphere impact human health, climate, and ecosystems through their critical contributions to secondary aerosol formation. Estimation of NH₃ emissions is associated with large uncertainties because of inadequate knowledge about agricultural sources. Here, we use satellite observations from the Infrared Atmospheric Sounding Interferometer (IASI) and simulations from the GEOS-Chem model to constrain global NH₃ emissions over the period of 2008-2018. We update the prior NH₃ emission fluxes with the ratio between biases in simulated NH₃ concentrations and effective NH₃ lifetimes against the loss of the NH$_x$ family. In contrast to about a factor of two discrepancies between top-down and bottom-up emissions found in previous studies, our method results in a global land NH₃ emission of 78 (70-92) Tg a^{-1}, ~30 % higher than the bottom-up estimates. Regionally, we find that the bottom-up inventory underestimates NH₃ emissions over South America and tropical Africa by 60-70 %, indicating under-representation of agricultural sources in these regions. We find a good agreement within 10 % between bottom-up and top-down estimates over the U.S., Europe, and eastern China. Our results also show significant increases in NH₃ emissions over India (13 % decade^{-1}), tropical Africa (33 % decade^{-1}), and South America (18 % decade^{-1}) during our study period, consistent with the intensifying agricultural activities in these regions in the past decade. We find that inclusion of sulfur dioxide (SO₂) column observed by satellite is crucial for more accurate inference of NH₃ emission trends over important source regions such as India and China where SO₂ emissions have changed rapidly in recent years.

1 Introduction

Emissions of ammonia (NH₃) to the atmosphere have critical implications for human health, climate, and ecosystems. As the main alkaline gas, NH₃ reacts with acidic products from precursors such as nitrogen oxides (NO$_x$) and sulfur dioxide (SO₂) to form fine particulate matter, which is a well-documented risk factor for human health, causing great welfare loss globally

33 (Erisman 2021; Gu et al., 2021). Particulate matter also affects the Earth's radiative balance by directly scattering incoming
34 radiation (Ma et al., 2012) and indirectly as cloud condensation nuclei (Höpfner et al., 2019). Additionally, both gas-phase
35 ammonia (NH_3) and aerosol-phase ammonium (NH_4^+) can deposit onto the surface of land and water through dry and wet
36 processes, and are associated with soil acidification (Zhao et al., 2009), ecosystem eutrophication (Dirnböck et al., 2013),
37 biodiversity loss (Stevens et al., 2010), and cropland nitrogen uptake (Liu et al., 2013).

38 NH_3 is emitted from a variety of anthropogenic and natural sources, including agriculture, industry, fossil fuel combustion,
39 biomass burning, natural soils, ocean, and wild animals (Behera et al., 2013). Among these, agricultural activities, mainly
40 livestock manure management and mineral fertilizer application, are the most important NH_3 sources, which account for ~70%
41 of the total NH_3 emissions globally (Bouwman et al., 1997; Sutton et al., 2013). NH_3 emissions can be estimated with a
42 bottom-up approach based on information of emission activities and emission factors (Hoesly et al., 2018; Crippa et al.,
43 2021). However, bottom-up estimates of NH_3 emissions are generally thought to be uncertain, relative to other pollutants that
44 are mainly from fossil fuel combustion sources (e.g., NO_x, CO). One of the challenges is that the intensity of agricultural
45 NH_3 emissions, emission factors, either from livestock or fertilizer, depends strongly on management and farming practices,
46 but this information is usually not widely available (Zhang et al., 2017). Furthermore, microbial activities that are
47 responsible for agricultural NH_3 emissions are highly variable and has a complex dependence on environmental conditions,
48 which is often inadequately captured by bottom-up approaches (Behera et al., 2013; Vira et al., 2021). In many cases,
49 emission factors used in bottom-up modelling are based on local studies that are not representative for the diversity of
50 conditions and are not dependent on meteorological parameters.

51 Top-down analyses of atmospheric observations (e.g., NH_3 concentrations or NH_4^+ depositional fluxes) provide an alternative
52 constraint on NH_3 emissions. For example, observations of NH_3 concentrations and NH_4^+ deposition fluxes from surface
53 networks can be used to infer regional NH_3 emission fluxes (e.g., Paulot et al., 2014). However, surface sites are often sparse,
54 especially in developing continents such as Africa and South America, limiting our capability to constrain NH_3 emissions
55 globally. The advent of satellite observations makes it possible to investigate long-term spatially resolved NH_3 emissions
56 from national, continental, to global scales. Van Damme et al. (2018) reported large NH_3 point sources across the globe that
57 are detected by the Infrared Atmospheric Sounding Interferometer (IASI) instrument but missing in the bottom-up
58 inventories. Studies have also applied satellite data (e.g., IASI and Cross-track Infrared Sounder (CrIS)) to study NH_3
59 emissions from important source regions, including the U.S. (Cao et al., 2020; Chen et al., 2021b), China (Zhang et al.,
60 2018), and Europe (Marais et al., 2021; van der Graaf et al., 2021). These regional studies show 20 % to 50 % differences
61 between top-down and bottom-up estimates of NH_3 emissions.

62 Compared to regional analyses, long-term global analyses of NH_3 emissions based on satellite observations are relatively
63 scarce (e.g., Evangeliou et al., 2021). This is partly because of the computational challenges arising from a full-fledged
64 inversion for a long period of time and over large spatial extents. In a recent study, Evangeliou et al. (2021) proposed a fast
65 top-down method, in which NH_3 emissions are computed as the ratio between NH_3 column observations and NH_3 lifetime.
66 This method relies on NH_3 lifetime diagnosed from a chemical transport model (CTM) and assumes a local mass balance.

67   Their analysis found a global NH$_3$ emission of around 180 Tg a^{-1}, which is roughly triple the widely used bottom-up

68   estimates (e.g., 62 Tg a^{-1} by the Community Emission Data System, CEDS). This large upward adjustment, if true, would

69   have huge implications for global reactive nitrogen cycles and indicate that our current understanding of global NH$_3$

70   emissions is seriously flawed.

71   In this paper, we examine if the large discrepancy between the bottom-up and top-down estimates is due to the methodology.

72   We refine the fast top-down approach by improving NH$_3$ lifetime diagnosis and partially accounting for the transport

73   contributions. We develop a series of data filtering procedures to exclude results that are not sufficiently constrained by

74   observations or affected by large deviations from the assumption of the fast top-down method. We apply the updated method

75   to IASI observations to derive the global distribution of NH$_3$ emissions fluxes from 2008 to 2018, and examine the impact of

76   the improved method on global NH$_3$ emission inferences.

77   **2 Methods**

78   **2.1 IASI observations**

79   We use 2008-2018 reanalyzed daily NH$_3$ total column retrievals (ANNI-NH$_3$-v3R) from the IASI on board Metop-A. The

80   IASI instrument measures the infrared radiation (645–2760 cm^{-1}) from Earth's surface and the atmosphere with a circular 12

81   km footprint at nadir (Clerbaux et al., 2009; Van Damme et al., 2017). The retrieval algorithm calculates the hyperspectral

82   range index from IASI spectra measurements (Van Damme et al. 2014) and converts it to the NH$_3$ total column density via

83   an artificial neural network (Whitburn et al., 2016; Franco et al., 2018). The retrieval uses consistent meteorological data

84   from the ERA5 reanalysis, so it is suitable for the analyses of inter-annual variability and long-term trends (Hersbach et al.,

85   2020). The ANNI-NH$_3$-v3R product, has been validated against in situ measurements and is shown to have a good regional

86   correlation (Guo et al., 2021; Van Damme et al., 2021). The dataset has been used in previous studies to estimate NH$_3$

87   emissions globally (e.g., Evangeliou et al., 2021) and regionally (e.g., Chen et al., 2021b; Marais et al., 2021).

88   Here we only use morning NH$_3$ data (around 9:30 local solar time) though IASI provides global coverage twice daily,

89   because of the better precision of morning observations resulting from favourable thermal contrast conditions (Clarisse et al.

90   2010). We filter out data with a cloud fraction greater than 10 % (Van Damme et al., 2018) and a skin temperature below

91   263 K (Van Damme et al., 2014). The skin temperature dataset is from ERA5 (Hersbach et al., 2020). To compare with

92   simulated NH$_3$ columns (see **Sect. 2.2**), we regrid and average monthly IASI NH$_3$ observations over land on the GEOS-

93   Chem 4° × 5° grid (**Fig. 1a**). To reduce uncertainty from sparse sampling, we further exclude grid cells with the number of

94   successful retrievals less than 800 in a month. We also test the choices of the threshold for 400 and 1200 per month in the

95   sensitivity calculations (**Table 1**, line 5-6). This criterion affects mainly high latitudes during wintertime, where snow

96   surfaces make it unfavourable for infrared measurements (**Fig. S1).**
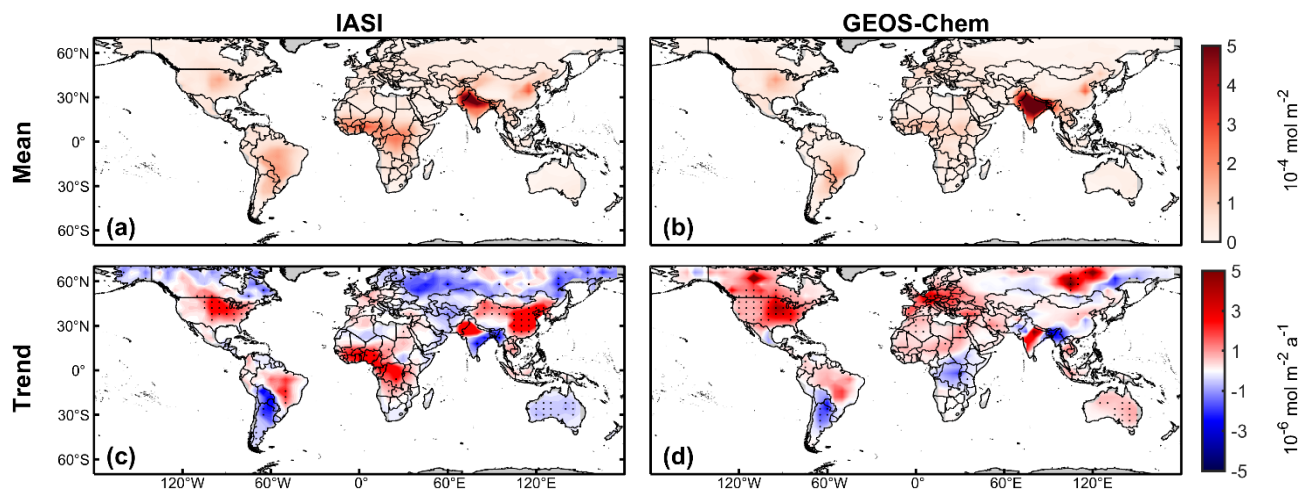
Figure 1. Spatial distribution of (a, c) IASI and (b, d) GEOS-Chem NH_3 column concentrations. (a, b) Mean and (c, d) linear trends within the **70**°N-**70**°S during 2008-2018. Dots in (c) and (d) indicate that linear trends are significant at the 95 % confidence levels. Linear trends are computed from the time series of annual averages.

2.2 GEOS-Chem simulations

We use the GEOS-Chem CTM v12.9.3 (10.5281/zenodo.3974569) to simulate global NH_3 concentrations. The GEOS-Chem model, driven by the MERRA-2 reanalyzed meteorology (Gelaro et al., 2017), simulates the tropospheric ozone–NOx–VOCs–aerosol chemistry at 4° × 5° resolution with 47 vertical layers (30 layers in the troposphere) (Bey et al., 2001; Park et al., 2004). The thermodynamic equilibrium between gas phase NH_3 and aerosol phase NH_4^+ is explicitly simulated by the ISORROPIA-II module in GEOS-Chem (Fountoukis & Nenes, 2007). The model also simulates the wet and dry deposition of NH_3 and NH_4^+, the terminal sinks of atmospheric NH_x ($\equiv NH_3 + NH_4^+$). Dry deposition is represented with a resistances-in-series scheme (Wesely, 2007) and wet deposition includes scavenging in convective updrafts and in- and below-cloud scavenging from large-scale precipitation (Wang et al., 2011; Amos et al., 2012). Anthropogenic emissions of simulated chemicals including those of NH_3 are taken from a global emission inventory CEDS (Hoesly et al., 2018), overridden by regional inventories in Canada (Air Pollutant Emission Inventory, APEI), the United States (2011 National Emissions Inventory, NEI-2011), Asia (MIX-Asia v1.1) (Li et al., 2017), and Africa (DICE-Africa) (Eloise Marais and Christine Wiedinmyer, 2016). Such compiled anthropogenic emissions only include incomplete information on inter-annual trends because inventories are not all available throughout the whole period. Anthropogenic emissions are essentially invariant after 2013 in our setup (**Fig. S2**). The general lack of trends in SO_2 emissions in the simulation, if not accounted for, may cause biases in inferred trends over regions such as India and China where SO_2 emissions have changed rapidly (Sun et al., 2018; Qu et al., 2019; Chen et al., 2021a). Fire emissions are from Global Fire Emissions Database (GFED4) (van der Werf et al., 2017), and biogenic VOC emissions are from the Model of Emissions of Gases and Aerosols from Nature (MEGAN) (Guenther et al., 2012). Temporal (seasonal and inter-annual) variations in fire and biogenic emissions are resolved by the inventories. Hereafter, we refer to NH_3 prior bottom-up emissions from this set of inventories as BUE1. For comparison, we

122 also use another set of bottom-up inventories which consist of EDGARv5.0 for anthropogenic emissions
123 (https://data.jrc.ec.europa.eu/collection/edgar, last access: 8 March 2022, Crippa et al., 2020), GFAS for fire emissions
124 (CAMS, https://apps.ecmwf.int/datasets/data/cams-gfas/, last access: 8 March 2022) (minor natural emissions are the same
125 as BUE1), which we denote as BUE2.

126 The GEOS-Chem simulation is conducted from 2008 to 2018 with an additional 1-month spin-up starting from December
127 2007. We sample the simulated NH_3 and NH_4^+ concentration fields between 9:00 to 10:00 local solar time, approximately the
128 IASI morning overpass time. To compare with the IASI NH_3 columns, we integrate the vertical profiles of simulated NH_3
129 concentrations by layer thickness. We note that the ANNI-NH_3-v3R retrieval does not provide averaging kernels (Whitburn
130 et al., 2016; Van Damme et al., 2021). However, Van Damme et al. (2018) reported the uncertainty in different vertical
131 profiles of individual NH_3 measurements to be 2 % $\pm$ 24 % (global average). Besides, we also archive depositional and
132 transport rates for NH_3 and NH_4^+, which are used in emission fluxes estimation. In addition, we perform GEOS-Chem
133 simulations in selected years (2008, 2013, 2018) to examine the validation and consistency of our top-down NH_3 emission
134 estimates with the ground-based measurements and IASI observations.

135 **2.3 NH_3 emission fluxes estimation**

136 We compute NH_3 fluxes ($\hat{E}_{NH_3}$, in molecules m^{-2} s^{-1}) in land grid cells for individual months from 2008 to 2018. We update
137 the prior model emission fluxes ($E_{NH_3,mod}$, in molecules m^{-2} s^{-1}) with a correction term positively proportional to the
138 difference of observed ($C_{NH_3,obs}$, in molecules m^{-2}) and simulated ($C_{NH_3,mod}$, in molecules m^{-2}) monthly averaged NH_3 total
139 column densities and inversely proportional to the lifetime of NH_3 ($\tau_{NH_3,mod}$, in s):

$$\hat{E}_{NH_3} = E_{NH_3,mod} + \frac{C_{NH_3,obs} - C_{NH_3,mod}}{\tau_{NH_3,mod}}, \tag{1}$$

141 where $\tau_{NH_3,mod}$ is computed as the ratio of the simulated NH_3 column and the sum of simulated loss rate of the NH_x family
142 ($NH_x \equiv NH_3 + NH_4^+$) through the dry and wet depositions of NH_3 ($D_{NH_3,mod}$, in molecules m^{-2} s^{-1}) and NH_4^+ ($D_{NH_4^+,mod}$, in
143 molecules m^{-2} s^{-1}):

$$\tau_{NH_3,mod} = \frac{C_{NH_3,mod}}{D_{NH_3,mod} + D_{NH_4^+,mod}}. \tag{2}$$

145 Here we calculate the lifetime of NH_3 with the loss of the NH_x family rather than that of NH_3, because of the fast
146 thermodynamic equilibrium between gas-phase NH_3 and aerosol/aqueous-phase NH_4^+, which implies that the conversion
147 from NH_3 to NH_4^+ is not a terminal loss for NH_3 from the atmosphere. The NH_3 lifetime may be underestimated over source
148 regions and overestimated over remote regions, if NH_3 to NH_4^+ conversions are treated as a terminal loss as in Evangeliou et
149 al. (2021) rather than a partition within a chemical family (NH_x) as in **Eq. (2)**.

150 In addition, our method linearizes the column-emission relationship at prior emissions as opposed to zero emissions in the
151 previous method (e.g., Evangeliou et al., 2021). Here, the baseline NH_3 column ($C_{NH_3,mod}$) simulated by the GEOS-Chem

152 model explicitly accounts for the non-local contribution of transport, while the correction to prior emissions is done only

153 locally, that is, the difference between $C_{\text{NH}_3,\text{obs}}$ and $C_{\text{NH}_3,\text{mod}}$ is attributed only to errors in local emissions without

154 accounting for the sensitivity to emissions from other grid cells. This hybrid approach can partially include the non-local

155 contribution from transport but still keeps the computation tractable for a long-term study such as this study, striking a trade-

156 off between the computational efficiency of a local mass balance method (e.g., Van Damme et al., 2018; Evangeliou et al.,

157 2021) and the accuracy of a full-fledged inversion, such as the 4D-Var method (e.g., Cao et al., 2020; Chen et al., 2021b).

158 The errors arising from local correction of NH_3 emissions are expected to be small in most cases, because the NH_3 lifetime is

159 short relative to a typical transport time across a $4° \times 5°$ grid cell on which emissions are estimated. To identify cases when

160 this error is not negligible, we apply a monthly NH_x budget analysis based on the GEOS-Chem simulation and exclude grid

161 cells from our analysis where transport dominates over local prior emissions or depositions in the monthly NH_x budget

162 (Transport/Emission>1 or Transport/Deposition>1) (**Fig. S3**).

163 Because rapid changes in SO_2 emissions in eastern China and India, particularly after 2012, are not captured by our prior

164 simulation (**Fig. S2**), the estimation of NH_3 emission trends using **Eq. (1)** may be biased over these regions. To address this

165 issue, we further modify **Eq. (1)** to include observed trends in SO_2 column concentrations:

$$166 \qquad \hat{E}_{\text{NH}_3,\text{SO}_2-\text{correct}} = E_{\text{NH}_3,\text{mod}} + \frac{C_{\text{NH}_3,\text{obs}} - C_{\text{NH}_3,\text{mod}} + 2\omega C_{SO_4^{2-},\text{mod}}}{\tau_{\text{NH}_3,\text{mod}}}, \qquad (3)$$

167 where ω (%) is the fractional changes of average SO_2 columns relative to the baseline year (i.e., 2012) over China or India

168 and $C_{SO_4^{2-},\text{mod}}$ (molecules m^{-2} s^{-1}) is the simulated column densities of aerosol sulfate. Here, we specify a linear trend of -5 %

169 a^{-1} for eastern China and 5 % a^{-1} for India between 2012 and 2018, based on values derived from the ozone monitoring

170 instrument (OMI) and Ozone Mapping and Profiler Suite (OMPS) observations (Wang and Wang, 2020; Liu et al., 2018).

171 We also test the impact of the uncertainty in ω on trend inferences over China and India. The factor 2 accounts for the fact

172 that two molecules of NH_3 are required to neutralize one molecule of H_2SO_4. **Eq. (3)** only applies when NH_3 is in excess, a

173 condition usually met in eastern China and India but not necessarily elsewhere (Lachatre et al., 2019; Acharja et al., 2022).

174 Therefore, we only apply **Eq. (3)** to eastern China and India to understand the impact of changing SO_2 emissions on the

175 inference of NH_3 emission trends. To use SO_2 observations systematically in NH_3 emission estimations requires further

176 investigations.

2.4 Uncertainty and sensitivity analysis

178 We perform a series of perturbation and sensitivity experiments to assess the uncertainty of our estimates (**Table 1**. We

179 perturb $C_{\text{NH}_3,\text{mod}}$ and $\tau_{\text{NH}_3,\text{mod}}$ in **Eq. (1)**. The perturbations to $\tau_{\text{NH}_3,\text{mod}}$ are set to be 50 % and 200 % (**Table 1**, Line 1-2).

180 The perturbation to $C_{\text{NH}_3,\text{mod}}$ is set to be the standard deviation of monthly mean column concentrations ($\sigma_{C,\text{obs}}$) (**Table 1**,

181 Line 3-4), which is given by:

182
$$\sigma_{C,obs} = \sqrt{\frac{\sum_{i=1}^{i=n}(\sigma_i \times \Omega_i)^2}{n-1}}, \tag{4}$$

183   where Ω_i (in mol m^{-2}) is the ith NH$_3$ column measurement out of a total number of n observations in a grid cell during a

184   month and σ_i is the relative error. We then use $\Omega \pm \sigma_{C,obs}$ to evaluate the effect of measurement errors in emission estimates

185   (**Table 1**, Line 3-4). We compute results with alternative data filtering parameters (**Table 1**, Line 5-8), including the

186   thresholds to exclude grid cells when the number of observations is too small (**Table 1**, line 5-6) and the local mass balance

187   assumption is potentially invalid (**Table 1**, Line 7-8). We also test if our trend inferences over China and India using Eq. (3)

188   is sensitive to uncertainty in observed trends in SO$_2$ concentrations (ω).

189   **Table 1.** Uncertainty and sensitivity analyses of top-down NH$_3$ emissions. Annual averaged NH$_3$ emissions are summed over global land
190   areas for 2008–2018.

	Parameter perturbed	Average emission (Tg a^{-1})
0	None [a] (TDE)	78
1	Halved NH$_3$ lifetime[b]	92
2	Doubled NH$_3$ lifetime[c]	70
3	Upper IASI column error	83
4	Lower IASI column error	72
5	Number of retrievals > 400[d]	81
6	Number of retrievals > 1200[e]	74
7	Transport/Emission < 0.2[f]	72
8	Transport/Emission < 5[g]	84

191   [a]Excluding a grid cell if retrieval number is less than 800 during a month, or transport dominates over emissions or

192   depositions in the simulated monthly NH$_3$ budget.

193   [b-c]The lifetime is 50 % and 200 % of values from Eq. (1), respectively.

194   [d-e]Monthly retrieval number threshold for including a grid cell is set to be 400 and 1200, respectively.

195   [f-g]Local budget ratio the threshold for including a grid cell is set to be 0.2 and 5, respectively.

196   **3 Results and discussion**

197   **3.1 Observed and simulated NH$_3$ concentrations**

198   **Fig. 1a and 1b** plot observed and simulated NH$_3$ total column concentrations averaged over 2008-2018. The GEOS-Chem

199   simulation generally reproduces the global distribution of NH$_3$ concentrations observed by the IASI instrument. Good

200   agreements (i.e., difference < 10 %) are found in the U.S., Europe, and southern South America. Meanwhile, the GEOS-

201 Chem model underestimates NH_3 concentrations in eastern China, northern South America, and tropical Africa by 20-120 %,
202 and overestimates in southern India by around 50 %, indicating biases in NH_3 emissions over these regions.

203 **Fig. 1c and 1d** show 2008-2018 linear trends in NH_3 column concentrations derived from the IASI observations and the
204 GEOS-Chem simulations. The linear trends are computed based on the time series of annual averages. The IASI trends
205 shown in Fig. 1c are in general consistent with a recent analysis by Van Damme et al. (2021). IASI observes a positive NH_3
206 concentration trend of 2.9 % a^{-1} over the U.S., and this trend is well captured by GEOS-Chem. Similarly, the observation and
207 the simulation agree on a dipole pattern in South America (i.e., positive trend in Brazil and negative trend in Argentina).
208 Because anthropogenic emissions over this region are set to be invariant in our simulation (**Fig. S2**), this agreement suggests
209 that these trends are due to meteorological conditions and/or fire emissions, rather than changes in anthropogenic emissions.
210 The satellite also observes significant positive trends in NH_3 concentrations over China (5.2 % a^{-1}) and tropical Africa (2.0 %
211 a^{-1}), but these trends are not reproduced in the simulation (0.3 % a^{-1} for China and 0.2 % a^{-1} for tropical Africa). These
212 simulation-observation differences can not only reflect discrepancies in the trends of anthropogenic NH_3 emissions, but also
213 be attributed to uncaptured changes in SO_2 and/or NO_x emissions in these regions. We also find that a positive NH_3
214 concentration trend over Europe appears in the simulation (3.0 % a^{-1}) but is much weaker (1.0 % a^{-1}) in the observation,
215 suggesting decreasing emissions after 2013. Satellite data shows positive NH_3 concentration trends in north-western India
216 but negative trends in in south-eastern India which are not reproduced by the simulation, though these trends over India are
217 mostly insignificant (at the 95 % confidence level) except for a few grid cells in the Southeast. Strong GEOS-Chem trends in
218 eastern Canada and Siberia result from large wildfires that occurred in the latter part of the study period. IASI trends in
219 northern boreal regions are less robust because of noisy and sparse measurements over high latitudes (**Fig. S1** and **Fig. S3**)

220 **3.2 NH_3 emissions inferred from IASI observations**

221 **Fig. 2** shows the spatial distributions of NH_3 emission fluxes and their 2008–2018 linear trends inferred from IASI
222 observations using the method described in **Sect. 2.3**. **Fig. 3** plots annual time series aggregated for seven selected regions.
223 The top-down emission (TDE) estimates suggest upward adjustments in NH_3 emissions over South America (SA) by 62 %,
224 tropical Africa (TA) by 69 %, and Central Asia (CA) by 327 %, relative to the prior inventory (BUE1), but downward
225 adjustments in NH_3 emissions by 14 % in India Peninsula (IP) and by 33 % in Canada. After accounting for the contributions
226 from natural emissions including fires, we find that most of these biases in NH_3 emissions can be attributed to anthropogenic
227 sources, except for Canada where the underestimation appears to relate to fire emissions. This result reflects a general
228 inadequate representation of agricultural and industrial emissions from developing continents in current global emission
229 inventories. The TDE finds good agreements with the BUE1 (difference within 10 %) over the U.S., Europe (EU), eastern
230 China (EC) and Australia.
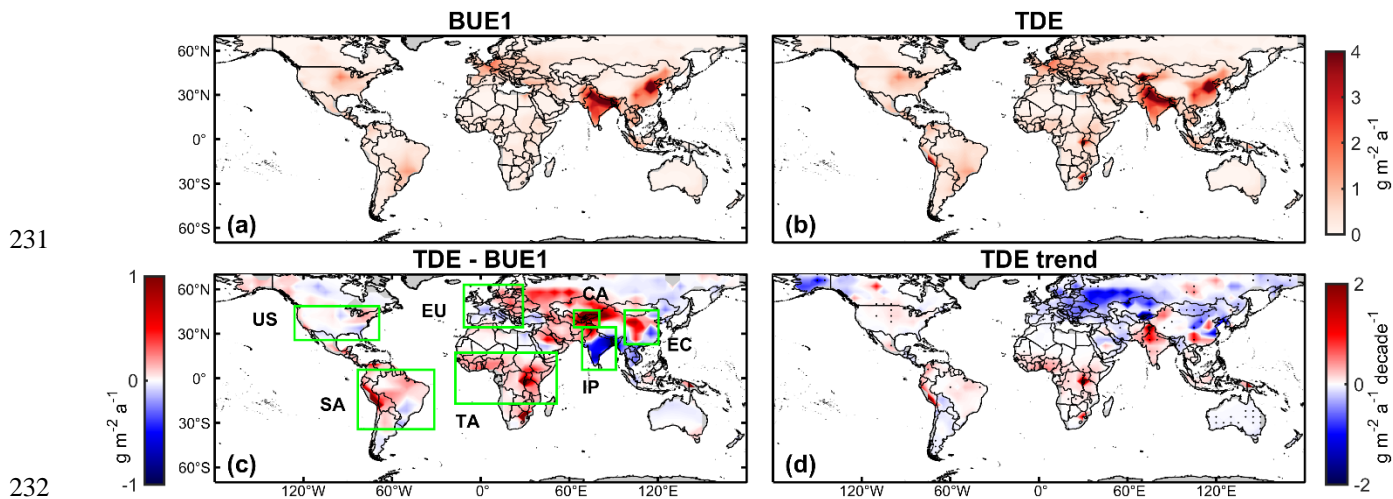
Figure 2. Spatial distribution of NH$_3$ emission fluxes during 2008-2018. (a) Bottom-up emissions (BUE1), (b) top-down emissions (TDE) inferred from IASI observations, (c) difference between TDE and BUE1 estimates and (d) emission trends derived from TDE estimates. Green boxes denote seven regions analyzed in Sect. 3.2. Top-down emission fluxes are computed with Eq. (1) except for IP and EC where Eq. (3) is applied. Linear trends are computed from the time series of annual averages. Dots in (d) represent significant linear trends at the 95 % confidence level.

In addition to the adjustments in average emissions, the TDE also detects changes in NH$_3$ emissions during the period of 2008-2018, as expressed in linear trends computed from annual time series. We find significant positive emission trends in SA (1.7 Tg a^{-1} decade^{-1} or 18 % decade^{-1}) and TA (2.8 Tg a^{-1} decade^{-1} or 33 % decade^{-1}) (**Fig. 3**). The large positive trends in TA are found around Lake Natron, consistent with Clarisse et al. (2019) (Fig. 2d). These increases in NH$_3$ emissions are concurrent with intensifying agricultural activities in these regions (Warner et al., 2017; E. Hickman et al., 2020), except for a 2010 peak over SA, which coincides with fires in savanna and evergreen forests there (Chen et al., 2013). Comparison with data from the Food and Agriculture Organization of the United Nations (FAO) (http://www.fao.org/faostat, last access: 7 May 2022) suggests that the increase in SA is driven primarily by growing application of synthetic fertilizer (55 % decade^{-1}), whereas the increase in TA is consistent with increasing manure amount (28 % decade^{-1}) from a growing livestock population (E. Hickman et al., 2021) (**Fig. 4**).

Our results infer large but variable trends over northern high latitudes (e.g., negative trends in Alaska, central Russia, and eastern Europe, but positive trends in Canada) (**Fig. 2d**). Because of large uncertainties associated with high-latitude observations and emission optimization, these trends are less robust but can be partly attributed to variations in fire activities. Decreases in Russia and eastern Europe are related to wildfire of boreal forests in early part of the study period (2008-2011) (Keywood et al., 2012; Warner et al., 2017), while emission increases in Canada is due to wildfire in the late part of the period (2013-2016 and 2017) (Pavlovic et al., 2016), as also shown in the prior fire inventory (GFED4) (**Fig. S4**). We also infer negative trends (-43 % decade^{-1}) in Australia, which are statistically significant, but the absolute magnitude of these trends is small (-0.03 g m^{-2} a^{-1} decade^{-1} in **Fig. 2d**). The TDE estimation does not find significant trends in NH$_3$ total emissions over the US and Central Asia.

257
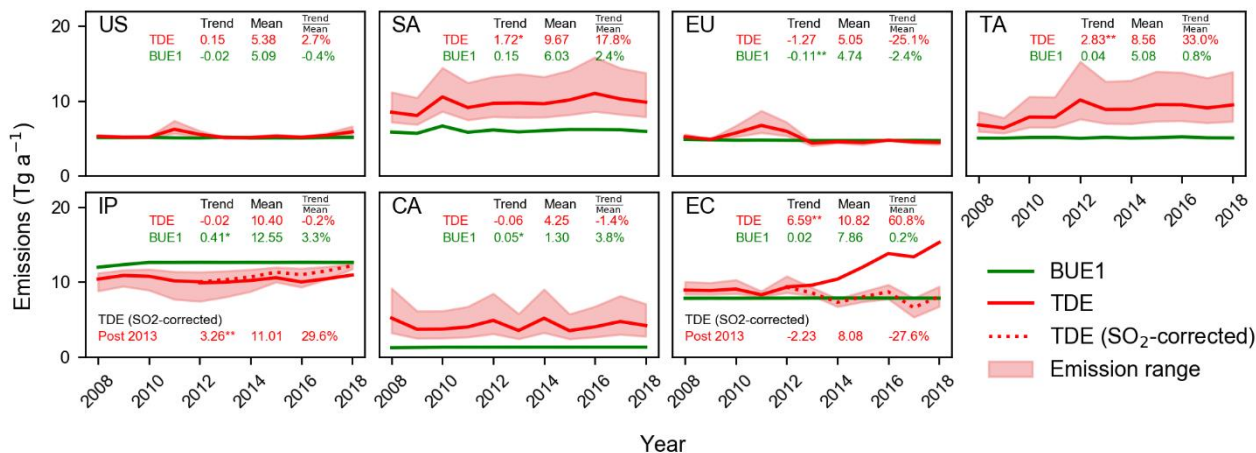
Figure 3. Annual NH_3 emissions for seven selected regions during 2008-2018. Shadings represent the upper and lower bounds derived from uncertainty analyses (see Sect. 2.4). Average annual emissions (Tg a^{-1}), absolute linear trends (Tg a^{-1} decade^{-1}) and relative trends (% decade^{-1}) for 2008-2018 are inset. The asterisk symbols '*' and '**' represent that linear trends are significant at the 95 % and 99 % confidence level, respectively. Red dashed lines represent top-down NH_3 emission estimates over IP and EC during 2013-2018, based on Eq. (3) that accounts for observed trends of SO_2 (denoted as "SO_2-corrected"). Statistics for this estimate are also inset. The prior inventory (BUE1) implemented in our simulation only partially account for inter-annual changes from bottom-up information (i.e., **Fig. 4**).

264
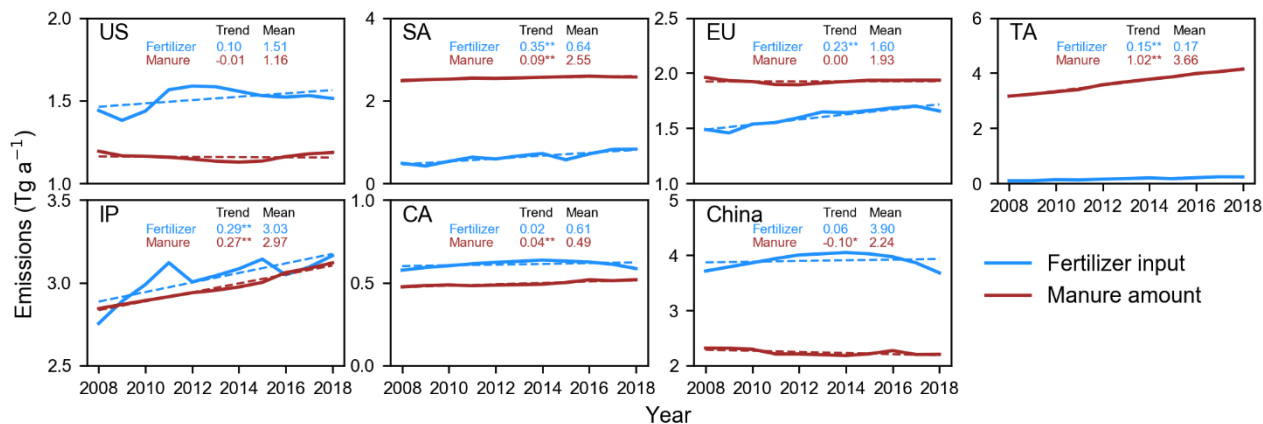
Figure 4. Synthetic fertilizer and livestock manure amount based on FAO reports (http://www.fao.org/faostat) during 2008-2018. To roughly compare the contribution from the two sectors, we convert FAO reported statistics to NH_3 emissions (Tg a^{-1}) by applying fixed emission factors of 13 % for manure N contents (Ma et al., 2020) and 17 % for synthetic fertilizer N contents (Riddick et al., 2016). Values of means (Tg a^{-1}) and linear trends (Tg a^{-1} decade^{-1}) are inset. Scales differ between panels.

3.3 Impact of changing SO_2 emissions on NH_3 emission trends over eastern China and India

Based on NH_3 column measurements (**Eq. (1)**), we also find a decadal increase of 61 % decade^{-1} (6.6 Tg a^{-1} decade^{-1}) in NH_3 emissions over eastern China (**Fig. 3**). This increase is especially large after 2013 and is driven mainly by increases of IASI NH_3 column concentration in eastern China (**Fig. 1c**). This large post-2013 increase is inconsistent with flat or even declining fertilizer input and manure amount (**Fig. 4**). On the other hand, we find no appreciable emission trend in IP (**Fig. 3**),

274 which appears to agree with relatively stable IASI NH_3 concentrations over the period (**Fig. 1c**) but is not supported by

275 increases in fertilizer applications and manure amount shown in the FAO report (**Fig. 4**).

276 An assumption underlying **Eq. (1)** is that the model simulation captures the partition between gas-phase NH_3 and aerosol-

277 phase NH_4^+. In addition to alkaline NH_3, the partition is also determined by the abundance of acids (e.g., H_2SO_4 and HNO_3).

278 Inaccurate emissions of their precursors (e.g., SO_2 and NO_2) in the model simulation, in particular over regions with

279 excessive NH_3, can lead to biases in simulating the NH_3-NH_4^+ partition. It is well known that SO_2 emissions in China have

280 decreased rapidly after 2013 because of stringent air pollution control measures (Sun et al., 2018; Zhai et al., 2021), while

281 SO_2 emissions from India have been increasing (Qu et al., 2019). But these regional trends are not captured in our prior

282 simulation because our simulation does not have annual-varying emission inventories for these regions (**Fig. S2**).

283 We find that the discrepancies between top-down (**Eq. 1**) and bottom-up estimates of emission trends over EC and IP can be

284 largely reconciled by including observed SO_2 column concentrations in the top-down calculation (**Eq. (3)**). By accounting

285 for OMI and OMPS observed SO_2 trends (Wang and Wang, 2020), we derive an overall decreasing trend in NH_3 emissions

286 in EC between 2013 and 2018 (-2.2 Tg a^{-1} decade^{-1}, -28 % decade^{-1}). This result suggests that observed increases in NH_3

287 columns over China are largely explained by decreases in SO_2 emissions (**Fig. 1** and **Fig. 3**), consistent with previous studies

288 (Fu et al., 2017; Liu et al., 2018; Lachatre et al., 2019; Chen et al., 2021a). Bottom-up inventories (e.g., MEIC v1.3, EDGAR

289 v5.0) also report stable or declining NH_3 emissions from China during the period (Li et al., 2017; Crippa et al., 2020).

290 Meanwhile, the revised method (**Eq. (3)**) finds a positive post-2013 trend (3.3 Tg a^{-1} decade^{-1}, 30 % yr^{-1}) in NH_3 emissions

291 over India. Compared with our original estimate using **Eq. (1)**, NH_3 emission trends derived with **Eq. (3)** (i.e., decrease in

292 China and increase in India after 2013) is more consistent with the bottom-up information of fertilizer input and manure

293 management (**Fig. 4**). This result demonstrates the potential of assimilating both NH_3 and SO_2 satellite observations in

294 constraining NH_3 emissions, which should be further explored in the future.

3.4 Global total NH_3 emissions

296 Integrating over land areas globally, our IASI-based TDE estimates of NH_3 is 78 (70-92) Tg a^{-1} (range of estimates from

297 uncertainty analysis, see **Table 1**) (**Fig. 5**). This result is about 20-40 % higher than bottom-up inventories (BUE1, 62 Tg a^{-1}

298 and BUE2, 56 Tg a^{-1}). In contrast, a previous study by Evangeliou et al. (2021) also based on the IASI data estimated a much

299 higher global NH_3 emission of 180 Tg a^{-1} (**Fig. 5**). One cause of the difference between the two IASI-based estimates is in

300 diagnosis of NH_3 lifetime from CTM. Evangeliou et al. (2021) treats conversion from NH_3 to NH_4^+ as a terminal loss and

301 diagnoses NH_3 lifetime averaged 11.6 ± 0.6 h globally from a CTM, which is close to a constant NH_3 lifetime (12 h)

302 assumed in Van Damme et al. (2018). In this study, we account for the fact that fast thermodynamic equilibrium can

303 establish between NH_3 and NH_4^+ so that NH_3 can only be terminally lost through the deposition of the NH_x family (**Eq. (2)**),

304 which yields a global averaged NH_3 lifetime of 21.2 ± 3.8 h (**Fig. 6**). This longer NH_3 lifetime implies a higher sensitivity of

305 NH_3 column density to NH_3 emissions, leading to a lower estimate for global NH_3 emissions. In addition, instead of locally

306 scaling observed NH_3 column by lifetime (Van Damme et al., 2018; Evangeliou et al, 2021; Marais et al., 2021), our method

307 (**Eq. (1)**) partially accounts for the non-local contribution from transport by including prior NH₃ columns from a full 3-D

308 simulation and using their difference from observed NH₃ columns to correct prior emissions, which prevents derivation of

309 large NH₃ emissions in remote regions where observed NH₃ concentrations are driven mainly by transport. Our data filtering

310 strategy (**Sect 2.1 and 2.2**) is also crucial to avoid spurious top-down results when satellite coverage is poor and the local

311 mass balance assumption does not hold.
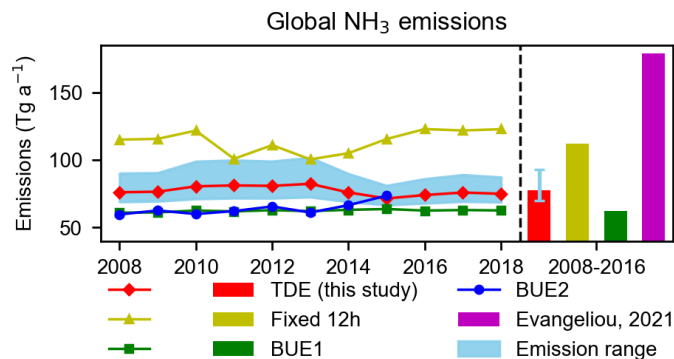
312

313 **Figure 5.** Comparison of our top-down NH₃ emission estimates (TDE) with other top-down (Fixed 12h and Evangeliou et al. (2021)) and
314 bottom-up (BUE1 and BUE2) results during 2008-2018. The red line and red bar represent central estimates of the TDE, and the blue
315 shaded area and the blue error bar indicate the uncertainty evaluated by our study (**Sect. 2.4**).
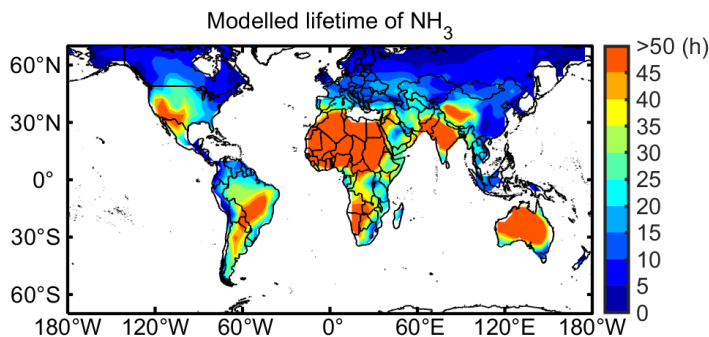
316

317 **Figure 6.** Spatial distribution of NH₃ lifetime (h) diagnosed from GEOS-Chem (Eq. (2)) within the **70°N-70°S** during 2008-2018.

318 **Fig. 6** shows the spatial variation in NH₃ lifetime diagnosed from the GEOS-Chem simulation. Short NH₃ lifetimes (< 10 h)

319 are found mainly in northern high latitudes. Short lifetime in eastern China is due to high wet NH_4^+ deposition velocity,

320 although some regional studies suggested an overestimation of deposition fluxes by the model especially in forest areas (e.g.,

321 Yangtze River basin) (Zhao et al., 2017; Xu et al., 2018). Very long NH₃ lifetime (> 100 h) occurs over Sahara and Australia,

322 where dry conditions result in slow wet deposition.

323 **3.5 Uncertainty evaluation**

324 We derive the uncertainty of top-down estimates from the perturbation tests in **Table 1**. **Fig. 7** shows the global spatial

325 distribution of annual average relative uncertainties of NH_3 emissions (ranges of perturbation tests divided by their averages).

326 The relative uncertainties are large (up to >100%) over northern latitudes, Central Asia, northern Africa, and South America,

327 where observations are often sparse. In comparison, the relative uncertainties are small (<40 %) in well-observed regions

328 including eastern China, northern India, Europe, and the U.S.
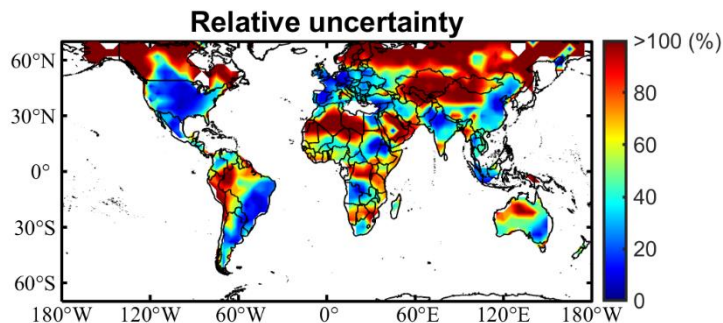
329

330 **Figure 7.** Spatial distribution of TDE relative uncertainty as the discrepancy of emission estimations in parameters perturbation (**Table 1**)
331 divided by the TDE average during 2008-2018.

332 Our fast top-down method (Eq. (1) and Eq. (3)) relies on simplification of NH_3 chemical and physical processes. Therefore,

333 it is not guaranteed that a simulation driven by TDE will generate results in improved agreement with IASI observations. We

334 evaluate the consistency of our results using full GEOS-Chem simulations in the selected years of 2008, 2013, and 2018.

335 Results are shown in **Fig. S5** (fractional bias, FB) and **Table S1** (number of valid grid cells, R^2, and root mean square error).

336 The GEOS-Chem simulations driven by the prior emissions (BUE1) tends to underestimate NH_3 column density (mean FB

337 ~-30%), while that driven by our TDE estimates achieves lower biases (mean FB ~10%), demonstrating the consistency of

338 our TDE results with IASI observations.

339 We also compare simulated surface NH_3 concentrations with independent ground-based measurements from North America

340 (AMoN, https://nadp.slh.wisc.edu/networks/ammonia-monitoring-network/, last access: 3 June 2022), Europe (EMEP,

341 http://ebas-data.nilu.no/, last access: 3 June 2022), and South-eastern Asia (EANET, http://ebas-data.nilu.no/, last access: 3

342 June 2022). **Fig. 8** shows the comparison by season. Only small adjustments are inferred by our satellite-based estimations in

343 these regions (i.e., North America, Europe, and South-eastern Asia). Thus, TDE and BUE1 show similar performance

344 against these ground measurements. Although the simulation can capture the site-to-site variations reasonably well,

345 simulated surface values are in general biased low compared to observations. This low bias is also reported in the evaluation

346 of previous IASI-based estimates (e.g., Evangeliou et al, 2021; Chen et al., 2021b), which may be due to several reasons, for

347 instance, systematic differences between satellite and surface measurements.
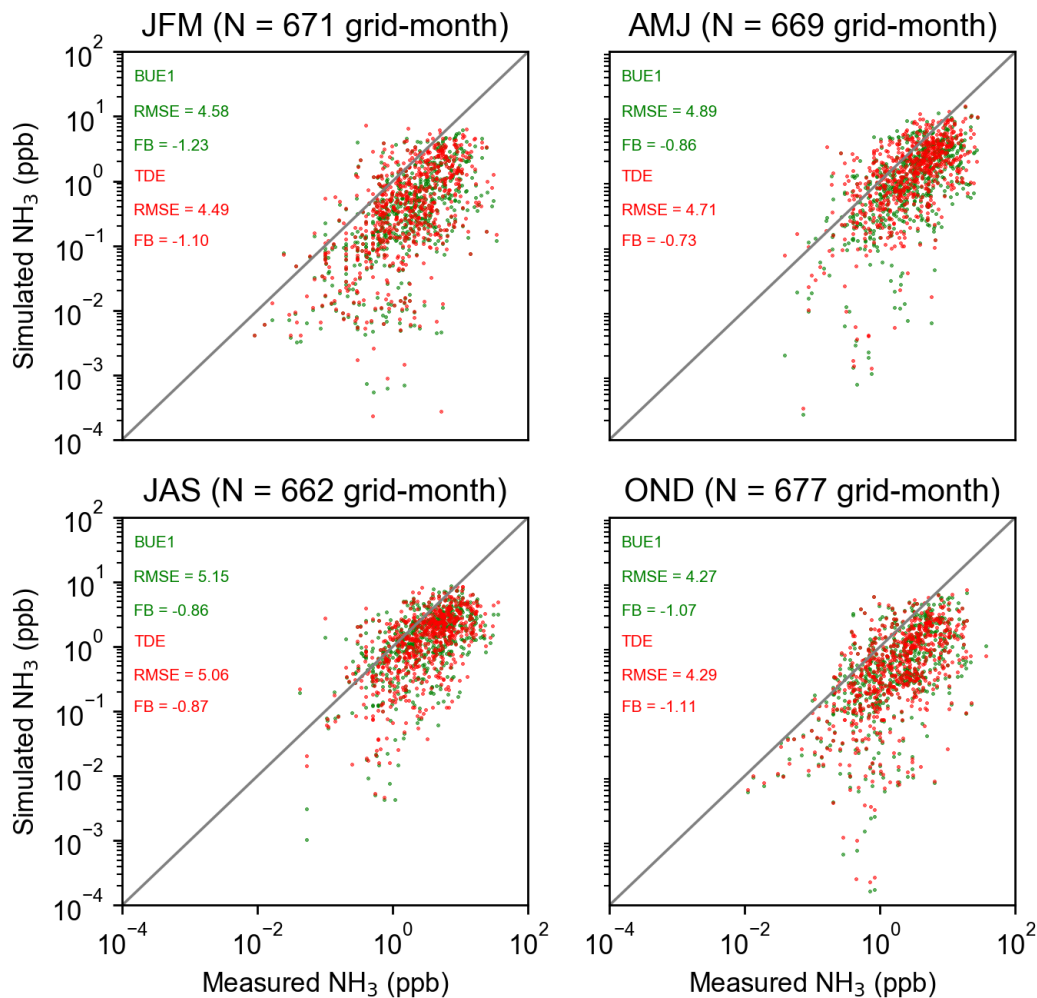
348

349 **Figure 8.** Validation of simulated NH₃ concentrations driven by BUE1 and TDE against ground-based measurements from AMoN, EMEP,
350 EANET for selected years (2008, 2013 and 2018) in four seasons (January-March, JFM; April-June, AMJ; July-September, JAS; October-
351 December, OND). Scatterplots are plotted in log scale and average RMSE (ppb) and FB (%) for each season are inset.

4 Conclusions

353 This study quantifies global ammonia (NH₃) fluxes monthly from 2008 to 2018 at 4° × 5° resolution, through a fast top-
354 down method that incorporates IASI satellite observations and GEOS-Chem model simulations. The top-down method
355 updates the prior NH₃ emissions with a correction term positively proportional to the difference of the observed and
356 simulated NH₃ concentrations, and inversely proportional to the lifetime diagnosed from a CTM. This method revises
357 previously proposed fast top-down methods in two aspects. First, we account for thermodynamic equilibrium within the NH$_x$
358 family in diagnosing NH₃ lifetime, while previous studies either assume a globally constant lifetime or treat conversion from
359 NH₃ to NH₄⁺ as a terminal sink. Second, our formulation linearizes the column-emission relationship at prior emissions as

360 opposed to zero emissions in the previous method, which in general reduces errors from the local mass balance
361 approximation. Another improvement is that we apply several data filtering procedures to exclude unreliable top-down
362 results that are not sufficiently constrained by observations or affected by large deviations from the local mass balance
363 assumption. The top-down method developed in this study is particularly useful for long-term global analysis of emission
364 trends, because it largely accounts for the impact of meteorology through the CTM simulation and requires only small
365 amount of computation relative to a full-fledged inversion.

366 We apply this improved fast top-down method to IASI NH_3 column observations from 2008 to 2018. We find that the BUE1
367 underestimates NH_3 emission over South America (62 %) and tropical Africa (69 %), but overestimates over India (14 %)
368 and Canada (33 %). The bottom-up inventory agrees with the top-down estimate over the U.S., Europe, and eastern China
369 (i.e., within 10 %). Our analysis also shows significant increases in India (13 % decade^{-1}), tropical Africa (33 % decade^{-1}),
370 and South America (18 % decade^{-1}) during the study period, consistent with intensifying agricultural activities over these
371 regions. An analysis of agricultural statistics suggests that the increase in tropical Africa is likely driven by growing
372 livestock population and that in South America by increasing fertilizer usage.

373 We show that large increases in NH_3 concentrations in eastern China is mainly driven by rapid decreases in SO_2 emissions in
374 recent years. By accounting for observed SO_2 columns, we find that NH_3 emissions from eastern China are significantly
375 decreasing during 2008-2018 (-19 % decade^{-1}), with a larger negative trend after 2013 (-28 % decade^{-1}), as compared to a
376 significant positive trend (61 % decade^{-1}) derived from assimilating only NH_3 data. Similarly, a lack of trend in observed
377 NH_3 concentrations over India is due to concurrent increases in SO_2 and NH_3 emissions. After including observed SO_2
378 columns in the calculation, we estimate a 13 % increase in NH_3 emissions over India, with a significant post-2013 positive
379 trend (30 % decade^{-1}). These results from assimilating both NH_3 and SO_2 data is more consistent with the agricultural
380 statistics in China and India. The multi-satellite (SO_2 and NH_3) method is only applied in India and China in this study. To
381 extend this idea globally requires development of formulations for varied sulfate-nitrate-ammonium aerosol regimes and
382 needs to be addressed in a future study.

383 Our estimate for global total NH_3 emission is 78 (70-92) Tg a^{-1}, about 30 % higher than the BUE1 estimate. This contrasts
384 with a much higher estimate (180 Tg a^{-1}) derived from Evangeliou et al. (2021) also using IASI data. The discrepancy can be
385 primarily attributed to a longer NH_3 lifetime (i.e., global average 21 h) diagnosed in our method, which represents a greater
386 sensitivity of NH_3 column to emissions, and a more conservative data filtering strategy, which removes potentially unreliable
387 top-down results. Our diagnosis of NH_3 lifetime is an improvement over Evangeliou et al. (2021), by accounting for the
388 thermodynamic equilibrium between gas phase NH_3 and aerosol phase NH_4^+ in our formula. We show with model
389 simulations, our top-down estimate achieves better consistency with IASI observations, compared to the bottom-up emission
390 inventory.

391

392 *Data availability.*

393 The IASI L2 ammonia satellite observations are available at the AERIS data infrastructure (https://iasi.aeris-data.fr/). The
394 ERA5 skin temperature and GFAS fire emission can be request through Copernicus Climate Data Store
395 (https://cds.climate.copernicus.eu/cdsapp#!/home). Agricultural data are available through Food and Agriculture
396 Organization of the United Nations (FAO) (http://www.fao.org/faostat). The GEOS-Chem model can be retrieved from
397 10.5281/zenodo.3974569. All the other data and scripts used for the present publication are available under MIT license on
398 GitHub: https://github.com/bnulzq/NH3-emission.git and can be obtained from corresponding author upon request.

399 *Author contributions.*

400 ZL and YZ designed the study. ZL performed the simulations and analyses and wrote and coordinated the paper. WC
401 contributed to the model simulations for consistency evaluation. LC, MVD, and PFC developed the IASI-NH3 satellite
402 product. ZL and YZ wrote the paper with inputs from all authors.

403 *Competing interests*

404 The contact author has declared that neither they nor their co-authors have any competing interests.

405 *Acknowledgements.*

406 This study is supported by Westlake University. We thank the High-Performance Computing Center of Westlake University
407 for the facility support and technical assistance. We acknowledge the AERIS data infrastructure https://www.aeris-data.fr for
408 providing access to the IASI data. The IASI L1c data are received through the EUMETCast near real-time data distribution
409 service. Research at ULB was supported by the Belgian State Federal Office for Scientific, Technical and Cultural Affairs
410 (Prodex HIRS) and the Air Liquide Foundation (TAPIR project). LC is Research Associate supported by the Belgian F.R.S.-
411 FNRS. Hersbach et al., (2020) was downloaded from the Copernicus Climate Change Service (C3S) Climate Data Store. The
412 results contain modified Copernicus Climate Change Service information 2020. Neither the European Commission nor
413 ECMWF is responsible for any use that may be made of the Copernicus information or data it contains. IASI is a join
414 mission of Eumetsat and the "Centre National d'Études Spatiales" (CNES, France). We acknowledge the constructive
415 comments and suggestions from Prof. Peter Hess from the Cornell University, Dr. Yi Wang from the University of Iowa, and
416 Dr. Shixian Zhai from Harvard University. We also acknowledge Dr. Nikolaos Evangeliou from Norwegian Institute for Air
417 Research for providing his NH_3 emission flux data and for discussions with ZL.

418 **References**

419 Acharja, P., Ali, K., Ghude, S. D., Sinha, V., Sinha, B., Kulkarni, R., Gultepe, I., and Rajeevan, M. N.:
420 Enhanced secondary aerosol formation driven by excess ammonia during fog episodes in Delhi, India,
421 Chemosphere, 289, 133155, 10.1016/j.chemosphere.2021.133155, 2022.

Amos, H. M., Jacob, D. J., Holmes, C. D., Fisher, J. A., Wang, Q., Yantosca, R. M., Corbitt, E. S., Galarneau, E., Rutter, A. P., Gustin, M. S., Steffen, A., Schauer, J. J., Graydon, J. A., Louis, V. L. S., Talbot, R. W., Edgerton, E. S., Zhang, Y., and Sunderland, E. M.: Gas-particle partitioning of atmospheric Hg(II) and its effect on global mercury deposition, Atmospheric Chemistry and Physics, 12, 591-603, 10.5194/acp-12-591-2012, 2012.

Behera, S. N., Sharma, M., Aneja, V. P., and Balasubramanian, R.: Ammonia in the atmosphere: a review on emission sources, atmospheric chemistry and deposition on terrestrial bodies, Environ Sci Pollut Res Int, 20, 8092-8131, 10.1007/s11356-013-2051-9, 2013.

Bey, I., Jacob, D. J., Yantosca, R. M., Logan, J. A., Field, B. D., Fiore, A. M., Li, Q., Liu, H. Y., Mickley, L. J., and Schultz, M. G.: Global modeling of tropospheric chemistry with assimilated meteorology: Model description and evaluation, Journal of Geophysical Research: Atmospheres, 106, 23073-23095, 10.1029/2001jd000807, 2001.

Bouwman, A. F., Lee, D. S., Asman, W. A. H., Dentener, F. J., Van Der Hoek, K. W., and Olivier, J. G. J.: A global high-resolution emission inventory for ammonia, Global Biogeochemical Cycles, 11, 561-587, 10.1029/97gb02266, 1997.

Cao, H., Henze, D. K., Shephard, M. W., Dammers, E., Cady-Pereira, K., Alvarado, M., Lonsdale, C., Luo, G., Yu, F., Zhu, L., Danielson, C. G., and Edgerton, E. S.: Inverse modeling of NH3 sources using CrIS remote sensing measurements, Environmental Research Letters, 15, 10.1088/1748-9326/abb5cc, 2020.

Chen, Y., Morton, D. C., Jin, Y., Collatz, G. J., Kasibhatla, P. S., van der Werf, G. R., DeFries, R. S., and Randerson, J. T.: Long-term trends and interannual variability of forest, savanna and agricultural fires in South America, Carbon Management, 4, 617-638, 10.4155/cmt.13.61, 2014.

Chen, Y., Zhang, L., Henze, D. K., Zhao, Y., Lu, X., Winiwarter, W., Guo, Y., Liu, X., Wen, Z., Pan, Y., and Song, Y.: Interannual variation of reactive nitrogen emissions and their impacts on PM2.5 air pollution in China during 2005–2015, Environmental Research Letters, 16, 10.1088/1748-9326/ac3695, 2021a.

Chen, Y., Shen, H., Kaiser, J., Hu, Y., Capps, S. L., Zhao, S., Hakami, A., Shih, J.-S., Pavur, G. K., Turner, M. D., Henze, D. K., Resler, J., Nenes, A., Napelenok, S. L., Bash, J. O., Fahey, K. M., Carmichael, G. R., Chai, T., Clarisse, L., Coheur, P.-F., Van Damme, M., and Russell, A. G.: High-resolution hybrid inversion of IASI ammonia columns to constrain US ammonia emissions using the CMAQ adjoint model, Atmospheric Chemistry and Physics, 21, 2067-2082, 10.5194/acp-21-2067-2021, 2021b.

Clarisse, L., Van Damme, M., Gardner, W., Coheur, P. F., Clerbaux, C., Whitburn, S., ... & Hurtmans, D. (2019). Atmospheric ammonia (NH$_3$) emanations from Lake Natron's saline mudflats. Scientific reports, 9(1), 1-12.

457 Clerbaux, C., Boynard, A., Clarisse, L., George, M., Hadji-Lazaro, J., Herbin, H., Hurtmans, D.,
458 Pommier, M., Razavi, A., Turquety, S. J. A. C., and Physics: Monitoring of atmospheric composition
459 using the thermal infrared IASI/MetOp sounder, Atmospheric Chemistry and Physics, 9, 6041-6054,
460 2009.

461 Crippa, M., Solazzo, E., Huang, G., Guizzardi, D., Koffi, E., Muntean, M., Schieberle, C., Friedrich, R.,
462 and Janssens-Maenhout, G.: High resolution temporal profiles in the Emissions Database for Global
463 Atmospheric Research, Sci Data, 7, 121, 10.1038/s41597-020-0462-2, 2020.

464 Dirnbock, T., Grandin, U., Bernhardt-Romermann, M., Beudert, B., Canullo, R., Forsius, M., Grabner,
465 M. T., Holmberg, M., Kleemola, S., Lundin, L., Mirtl, M., Neumann, M., Pompei, E., Salemaa, M.,
466 Starlinger, F., Staszewski, T., and Uzieblo, A. K.: Forest floor vegetation response to nitrogen
467 deposition in Europe, Glob Chang Biol, 20, 429-440, 10.1111/gcb.12440, 2014.

468 Erisman, J. W. J. S.: How ammonia feeds and pollutes the world, Science, 374, 685-686, 2021.

469 Evangeliou, N., Balkanski, Y., Eckhardt, S., Cozic, A., Van Damme, M., Coheur, P.-F., Clarisse, L.,
470 Shephard, M. W., Cady-Pereira, K. E., and Hauglustaine, D.: 10-year satellite-constrained fluxes of
471 ammonia improve performance of chemistry transport models, Atmospheric Chemistry and Physics, 21,
472 4431-4451, 10.5194/acp-21-4431-2021, 2021.

473 Fountoukis, C., Nenes, A. J. A. C., and Physics: ISORROPIA II: a computationally efficient
474 thermodynamic equilibrium model for K+–Ca 2+–Mg 2+–NH 4+–Na+–SO 4 2−–NO 3−–Cl−–H 2 O
475 aerosols, Atmospheric Chemistry and Physics, 7, 4639-4659, 2007.

476 Franco, B., Clarisse, L., Stavrakou, T., Müller, J. F., Van Damme, M., Whitburn, S., Hadji‐Lazaro, J.,
477 Hurtmans, D., Taraborrelli, D., Clerbaux, C., and Coheur, P. F.: A General Framework for Global
478 Retrievals of Trace Gases From IASI: Application to Methanol, Formic Acid, and PAN, Journal of
479 Geophysical Research: Atmospheres, 123, 10.1029/2018jd029633, 2018.

480 Fu, X., Wang, S., Xing, J., Zhang, X., Wang, T., and Hao, J.: Increasing Ammonia Concentrations
481 Reduce the Effectiveness of Particle Pollution Control Achieved via SO2 and NOX Emissions
482 Reduction in East China, Environmental Science & Technology Letters, 4, 221-227,
483 10.1021/acs.estlett.7b00143, 2017.

484 Gelaro, R., McCarty, W., Suarez, M. J., Todling, R., Molod, A., Takacs, L., Randles, C., Darmenov, A.,
485 Bosilovich, M. G., Reichle, R., Wargan, K., Coy, L., Cullather, R., Draper, C., Akella, S., Buchard, V.,
486 Conaty, A., da Silva, A., Gu, W., Kim, G. K., Koster, R., Lucchesi, R., Merkova, D., Nielsen, J. E.,
487 Partyka, G., Pawson, S., Putman, W., Rienecker, M., Schubert, S. D., Sienkiewicz, M., and Zhao, B.:
488 The Modern-Era Retrospective Analysis for Research and Applications, Version 2 (MERRA-2), J Clim,
489 Volume 30, 5419-5454, 10.1175/JCLI-D-16-0758.1, 2017.

490 Gu, B., Zhang, L., Van Dingenen, R., Vieno, M., Van Grinsven, H. J., Zhang, X., Zhang, S., Chen, Y.,
491 Wang, S., and Ren, C. J. S.: Abating ammonia is more cost-effective than nitrogen oxides for mitigating
492 PM2. 5 air pollution, Science, 374, 758-762, 2021.

Guenther, A. B., Jiang, X., Heald, C. L., Sakulyanontvittaya, T., Duhl, T., Emmons, L. K., and Wang, X.: The Model of Emissions of Gases and Aerosols from Nature version 2.1 (MEGAN2.1): an extended and updated framework for modeling biogenic emissions, Geoscientific Model Development, 5, 1471-1492, 10.5194/gmd-5-1471-2012, 2012.

Guo, X., Wang, R., Pan, D., Zondlo, M. A., Clarisse, L., Van Damme, M., Whitburn, S., Coheur, P. F., Clerbaux, C., Franco, B., Golston, L. M., Wendt, L., Sun, K., Tao, L., Miller, D., Mikoviny, T., Müller, M., Wisthaler, A., Tevlin, A. G., Murphy, J. G., Nowak, J. B., Roscioli, J. R., Volkamer, R., Kille, N., Neuman, J. A., Eilerman, S. J., Crawford, J. H., Yacovitch, T. I., Barrick, J. D., and Scarino, A. J.: Validation of IASI Satellite Ammonia Observations at the Pixel Scale Using In Situ Vertical Profiles, Journal of Geophysical Research: Atmospheres, 126, 10.1029/2020jd033475, 2021.

Hersbach, H., Bell, B., Berrisford, P., Hirahara, S., Horányi, A., Muñoz‐Sabater, J., Nicolas, J., Peubey, C., Radu, R., Schepers, D., Simmons, A., Soci, C., Abdalla, S., Abellan, X., Balsamo, G., Bechtold, P., Biavati, G., Bidlot, J., Bonavita, M., Chiara, G., Dahlgren, P., Dee, D., Diamantakis, M., Dragani, R., Flemming, J., Forbes, R., Fuentes, M., Geer, A., Haimberger, L., Healy, S., Hogan, R. J., Hólm, E., Janisková, M., Keeley, S., Laloyaux, P., Lopez, P., Lupu, C., Radnoti, G., Rosnay, P., Rozum, I., Vamborg, F., Villaume, S., and Thépaut, J. N.: The ERA5 global reanalysis, Quarterly Journal of the Royal Meteorological Society, 146, 1999-2049, 10.1002/qj.3803, 2020.

Hickman, J. E., Andela, N., Tsigaridis, K., Galy-Lacaux, C., Ossohou, M., and Bauer, S. E.: Reductions in NO2 burden over north equatorial Africa from decline in biomass burning in spite of growing fossil fuel use, 2005 to 2017, Proc Natl Acad Sci U S A, 118, 10.1073/pnas.2002579118, 2021a.

Hickman, J. E., Andela, N., Dammers, E., Clarisse, L., Coheur, P.-F., Van Damme, M., Di Vittorio, C. A., Ossohou, M., Galy-Lacaux, C., Tsigaridis, K., and Bauer, S. E.: Changes in biomass burning, wetland extent, or agriculture drive atmospheric NH₃; trends in select African regions, Atmospheric Chemistry and Physics, 21, 16277-16291, 10.5194/acp-21-16277-2021, 2021b.

Hoesly, R. M., Smith, S. J., Feng, L., Klimont, Z., Janssens-Maenhout, G., Pitkanen, T., Seibert, J. J., Vu, L., Andres, R. J., Bolt, R. M., Bond, T. C., Dawidowski, L., Kholod, N., Kurokawa, J.-i., Li, M., Liu, L., Lu, Z., Moura, M. C. P., O'Rourke, P. R., and Zhang, Q.: Historical (1750–2014) anthropogenic emissions of reactive gases and aerosols from the Community Emissions Data System (CEDS), Geoscientific Model Development, 11, 369-408, 10.5194/gmd-11-369-2018, 2018.

Höpfner, M., Ungermann, J., Borrmann, S., Wagner, R., Spang, R., Riese, M., Stiller, G., Appel, O., Batenburg, A. M., Bucci, S., Cairo, F., Dragoneas, A., Friedl-Vallon, F., Hünig, A., Johansson, S., Krasauskas, L., Legras, B., Leisner, T., Mahnke, C., Möhler, O., Molleker, S., Müller, R., Neubert, T., Orphal, J., Preusse, P., Rex, M., Saathoff, H., Stroh, F., Weigel, R., and Wohltmann, I.: Ammonium nitrate particles formed in upper troposphere from ground ammonia sources during Asian monsoons, Nature Geoscience, 12, 608-612, 10.1038/s41561-019-0385-8, 2019.

Keywood, M., Kanakidou, M., Stohl, A., Dentener, F., Grassi, G., Meyer, C. P., Torseth, K., Edwards, D., Thompson, A. M., Lohmann, U., and Burrows, J.: Fire in the Air: Biomass Burning Impacts in a

Changing Climate, Critical Reviews in Environmental Science and Technology, 43, 40-83, 10.1080/10643389.2011.604248, 2011.

Lachatre, M., Fortems-Cheiney, A., Foret, G., Siour, G., Dufour, G., Clarisse, L., Clerbaux, C., Coheur, P.-F., Van Damme, M., and Beekmann, M.: The unintended consequence of SO_2 and NO_2; regulations over China: increase of ammonia levels and impact on $PM_{2.5}$; concentrations, Atmospheric Chemistry and Physics, 19, 6701-6716, 10.5194/acp-19-6701-2019, 2019.

Li, M., Zhang, Q., Kurokawa, J.-i., Woo, J.-H., He, K., Lu, Z., Ohara, T., Song, Y., Streets, D. G., Carmichael, G. R., Cheng, Y., Hong, C., Huo, H., Jiang, X., Kang, S., Liu, F., Su, H., and Zheng, B.: MIX: a mosaic Asian anthropogenic emission inventory under the international collaboration framework of the MICS-Asia and HTAP, Atmospheric Chemistry and Physics, 17, 935-963, 10.5194/acp-17-935-2017, 2017.

Liu, M., Huang, X., Song, Y., Xu, T., Wang, S., Wu, Z., Hu, M., Zhang, L., Zhang, Q., Pan, Y., Liu, X., and Zhu, T.: Rapid SO_2; emission reductions significantly increase tropospheric ammonia concentrations over the North China Plain, Atmospheric Chemistry and Physics, 18, 17933-17943, 10.5194/acp-18-17933-2018, 2018.

Liu, X., Zhang, Y., Han, W., Tang, A., Shen, J., Cui, Z., Vitousek, P., Erisman, J. W., Goulding, K., Christie, P., Fangmeier, A., and Zhang, F.: Enhanced nitrogen deposition over China, Nature, 494, 459-462, 10.1038/nature11917, 2013.

Ma, R., Zou, J., Han, Z., Yu, K., Wu, S., Li, Z., Liu, S., Niu, S., Horwath, W. R., and Zhu-Barker, X.: Global soil-derived ammonia emissions from agricultural nitrogen fertilizer application: A refinement based on regional and crop-specific emission factors, Glob Chang Biol, 27, 855-867, 10.1111/gcb.15437, 2021.

Ma, X., Yu, F., and Luo, G.: Aerosol direct radiative forcing based on GEOS-Chem-APM and uncertainties, Atmospheric Chemistry and Physics, 12, 5563-5581, 10.5194/acp-12-5563-2012, 2012.

Marais, E. A. and Wiedinmyer, C.: Air Quality Impact of Diffuse and Inefficient Combustion Emissions in Africa (DICE-Africa), Environ Sci Technol, 50, 10739-10745, 10.1021/acs.est.6b02602, 2016.

Marais, E. A., Pandey, A. K., Van Damme, M., Clarisse, L., Coheur, P. F., Shephard, M. W., Cady‐Pereira, K. E., Misselbrook, T., Zhu, L., Luo, G., and Yu, F.: UK Ammonia Emissions Estimated With Satellite Observations and GEOS‐Chem, Journal of Geophysical Research: Atmospheres, 126, 10.1029/2021jd035237, 2021.

Park, R. J.: Natural and transboundary pollution influences on sulfate-nitrate-ammonium aerosols in the United States: Implications for policy, Journal of Geophysical Research, 109, 10.1029/2003jd004473, 2004.

Paulot, F., Jacob, D. J., Pinder, R. W., Bash, J. O., Travis, K., and Henze, D. K.: Ammonia emissions in the United States, European Union, and China derived by high-resolution inversion of ammonium wet

565 deposition data: Interpretation with a new agricultural emissions inventory (MASAGE_NH3), Journal
566 of Geophysical Research: Atmospheres, 119, 4343-4364, 10.1002/2013jd021130, 2014.

567 Pavlovic, R., Chen, J., Anderson, K., Moran, M. D., Beaulieu, P. A., Davignon, D., and Cousineau, S.:
568 The FireWork air quality forecast system with near-real-time biomass burning emissions: Recent
569 developments and evaluation of performance for the 2015 North American wildfire season, J Air Waste
570 Manag Assoc, 66, 819-841, 10.1080/10962247.2016.1158214, 2016.

571 Qu, Z., Henze, D. K., Li, C., Theys, N., Wang, Y., Wang, J., Wang, W., Han, J., Shim, C., Dickerson, R.
572 R., and Ren, X.: SO2 Emission Estimates Using OMI SO2 Retrievals for 2005-2017, J Geophys Res
573 Atmos, 124, 8336-8359, 10.1029/2019JD030243, 2019.

574 Riddick, S., Ward, D., Hess, P., Mahowald, N., Massad, R., and Holland, E.: Estimate of changes in
575 agricultural terrestrial nitrogen pathways and ammonia emissions from 1850 to present in the
576 Community Earth System Model, Biogeosciences, 13, 3397-3426, 10.5194/bg-13-3397-2016, 2016.

577 Schiferl, L. D., Heald, C. L., Van Damme, M., Clarisse, L., Clerbaux, C., Coheur, P.-F., Nowak, J. B.,
578 Neuman, J. A., Herndon, S. C., Roscioli, J. R., and Eilerman, S. J.: Interannual variability of ammonia
579 concentrations over the United States:

580 sources and implications, Atmospheric Chemistry and Physics, 16, 12305-12328, 10.5194/acp-16-
581 12305-2016, 2016.

582 Stevens, C. J., Dupre, C., Dorland, E., Gaudnik, C., Gowing, D. J., Bleeker, A., Diekmann, M., Alard,
583 D., Bobbink, R., Fowler, D., Corcket, E., Mountford, J. O., Vandvik, V., Aarrestad, P. A., Muller, S.,
584 and Dise, N. B.: Nitrogen deposition threatens species richness of grasslands across Europe, Environ
585 Pollut, 158, 2940-2945, 10.1016/j.envpol.2010.06.006, 2010.

586 Sun, W., Shao, M., Granier, C., Liu, Y., Ye, C. S., and Zheng, J. Y.: Long-Term Trends of
587 Anthropogenic SO2, NOx, CO, and NMVOCs Emissions in China, Earth's Future, 6, 1112-1133,
588 10.1029/2018ef000822, 2018.

589 Sutton, M. A., Reis, S., Riddick, S. N., Dragosits, U., Nemitz, E., Theobald, M. R., Tang, Y. S., Braban,
590 C. F., Vieno, M., Dore, A. J., Mitchell, R. F., Wanless, S., Daunt, F., Fowler, D., Blackall, T. D.,
591 Milford, C., Flechard, C. R., Loubet, B., Massad, R., Cellier, P., Personne, E., Coheur, P. F., Clarisse, L.,
592 Van Damme, M., Ngadi, Y., Clerbaux, C., Skjoth, C. A., Geels, C., Hertel, O., Wichink Kruit, R. J.,
593 Pinder, R. W., Bash, J. O., Walker, J. T., Simpson, D., Horvath, L., Misselbrook, T. H., Bleeker, A.,
594 Dentener, F., and de Vries, W.: Towards a climate-dependent paradigm of ammonia emission and
595 deposition, Philos Trans R Soc Lond B Biol Sci, 368, 20130166, 10.1098/rstb.2013.0166, 2013.

596 Van Damme, M., Whitburn, S., Clarisse, L., Clerbaux, C., Hurtmans, D., and Coheur, P.-F.: Version 2
597 of the IASI NH$_3$; neural network retrieval algorithm: near-real-time and reanalysed datasets,
598 Atmospheric Measurement Techniques, 10, 4905-4914, 10.5194/amt-10-4905-2017, 2017.

599 Van Damme, M., Clarisse, L., Whitburn, S., Hadji-Lazaro, J., Hurtmans, D., Clerbaux, C., and Coheur,
600 P. F.: Industrial and agricultural ammonia point sources exposed, Nature, 564, 99-103, 10.1038/s41586-
601 018-0747-1, 2018.

602 Van Damme, M., Clarisse, L., Heald, C. L., Hurtmans, D., Ngadi, Y., Clerbaux, C., Dolman, A. J.,
603 Erisman, J. W., and Coheur, P. F.: Global distributions, time series and error characterization of
604 atmospheric ammonia (NH_3) from IASI satellite observations, Atmospheric Chemistry and Physics, 14,
605 2905-2922, 10.5194/acp-14-2905-2014, 2014.

606 Van Damme, M., Clarisse, L., Franco, B., Sutton, M. A., Erisman, J. W., Wichink Kruit, R., van Zanten,
607 M., Whitburn, S., Hadji-Lazaro, J., Hurtmans, D., Clerbaux, C., and Coheur, P.-F.: Global, regional and
608 national trends of atmospheric ammonia derived from a decadal (2008–2018) satellite record,
609 Environmental Research Letters, 16, 10.1088/1748-9326/abd5e0, 2021.

610 Van Damme, M., Clarisse, L., Dammers, E., Liu, X., Nowak, J. B., Clerbaux, C., Flechard, C. R., Galy-
611 Lacaux, C., Xu, W., Neuman, J. A., Tang, Y. S., Sutton, M. A., Erisman, J. W., and Coheur, P. F.:
612 Towards validation of ammonia (NH_3) measurements from the IASI satellite, Atmospheric
613 Measurement Techniques, 8, 1575-1591, 10.5194/amt-8-1575-2015, 2015.

614 van der Graaf, S., Dammers, E., Segers, A., Kranenburg, R., Schaap, M., Shephard, M. W., and Erisman,
615 J. W.: Data assimilation of CrIS NH_3; satellite observations for improving spatiotemporal NH_3;
616 distributions in LOTOS-EUROS, Atmospheric Chemistry and Physics, 22, 951-972, 10.5194/acp-22-
617 951-2022, 2022.

618 van der Werf, G. R., Randerson, J. T., Giglio, L., van Leeuwen, T. T., Chen, Y., Rogers, B. M., Mu, M.,
619 van Marle, M. J. E., Morton, D. C., Collatz, G. J., Yokelson, R. J., and Kasibhatla, P. S.: Global fire
620 emissions estimates during 1997–2016, Earth System Science Data, 9, 697-720, 10.5194/essd-9-697-
621 2017, 2017.

622 Vira, J., Hess, P., Ossohou, M., and Galy-Lacaux, C., 10.5194/acp-2021-538,

623 Wang, Q., Jacob, D. J., Fisher, J. A., Mao, J., Leibensperger, E. M., Carouge, C. C., Le Sager, P.,
624 Kondo, Y., Jimenez, J. L., Cubison, M. J., and Doherty, S. J.: Sources of carbonaceous aerosols and
625 deposited black carbon in the Arctic in winter-spring: implications for radiative forcing, Atmospheric
626 Chemistry and Physics, 11, 12453-12473, 10.5194/acp-11-12453-2011, 2011.

627 Wang, Y. and Wang, J.: Tropospheric SO2 and NO2 in 2012–2018: Contrasting views of two sensors
628 (OMI and OMPS) from space, Atmospheric Environment, 223, 10.1016/j.atmosenv.2019.117214, 2020.

629 Warner, J. X., Dickerson, R. R., Wei, Z., Strow, L. L., Wang, Y., and Liang, Q.: Increased atmospheric
630 ammonia over the world's major agricultural areas detected from space, Geophys Res Lett, 44, 2875-
631 2884, 10.1002/2016GL072305, 2017.

632 Wesely, M.: Parameterization of surface resistances to gaseous dry deposition in regional-scale
633 numerical models☆, Atmospheric Environment, 41, 52-63, 10.1016/j.atmosenv.2007.10.058, 2007.

634 Whitburn, S., Van Damme, M., Clarisse, L., Bauduin, S., Heald, C. L., Hadji-Lazaro, J., Hurtmans, D.,
635 Zondlo, M. A., Clerbaux, C., and Coheur, P. F.: A flexible and robust neural network IASI-
636 NH3retrieval algorithm, Journal of Geophysical Research: Atmospheres, 121, 6581-6599,
637 10.1002/2016jd024828, 2016.

638 Xu, W., Zhao, Y., Liu, X., Dore, A. J., Zhang, L., Liu, L., and Cheng, M.: Atmospheric nitrogen
639 deposition in the Yangtze River basin: Spatial pattern and source attribution, Environ Pollut, 232, 546-
640 555, 10.1016/j.envpol.2017.09.086, 2018.

641 Zhai, S., Jacob, D. J., Wang, X., Liu, Z., Wen, T., Shah, V., Li, K., Moch, J. M., Bates, K. H., Song, S.,
642 Shen, L., Zhang, Y., Luo, G., Yu, F., Sun, Y., Wang, L., Qi, M., Tao, J., Gui, K., Xu, H., Zhang, Q.,
643 Zhao, T., Wang, Y., Lee, H. C., Choi, H., and Liao, H.: Control of particulate nitrate air pollution in
644 China, Nature Geoscience, 14, 389-395, 10.1038/s41561-021-00726-z, 2021.

645 Zhang, L., Chen, Y., Zhao, Y., Henze, D. K., Zhu, L., Song, Y., Paulot, F., Liu, X., Pan, Y., Lin, Y., and
646 Huang, B.: Agricultural ammonia emissions in China: reconciling bottom-up and top-down estimates,
647 Atmospheric Chemistry and Physics, 18, 339-355, 10.5194/acp-18-339-2018, 2018.

648 Zhang, X., Wu, Y., Liu, X., Reis, S., Jin, J., Dragosits, U., Van Damme, M., Clarisse, L., Whitburn, S.,
649 Coheur, P. F., and Gu, B.: Ammonia Emissions May Be Substantially Underestimated in China,
650 Environ Sci Technol, 51, 12089-12096, 10.1021/acs.est.7b02171, 2017.

651 Zhao, Y., Duan, L., Xing, J., Larssen, T., Nielsen, C. P., and Hao, J.: Soil acidification in China: is
652 controlling SO2 emissions enough?, 2009.

653 Zhao, Y., Zhang, L., Chen, Y., Liu, X., Xu, W., Pan, Y., and Duan, L.: Atmospheric nitrogen deposition
654 to China: A model analysis on nitrogen budget and critical load exceedance, Atmospheric Environment,
655 153, 32-40, 10.1016/j.atmosenv.2017.01.018, 2017.

656